PCCP

Revisiting Thiophosphate Pb$_3$P$_2$S$_8$: A Multifunctional Material Combining a Nonlinear Optical Response and Photocurrent Response

SCHOLARONE™
Manuscripts

Revisiting Thiophosphate Pb$_3$P$_2$S$_8$: A Multifunctional Material Combining a Nonlinear Optical Response and Photocurrent Response

Bingheng Ji [a], Elizabeth Guderjahn [a], Kui Wu [b], Tajamul Hussain Syed[c], Wei Wei [c], Bingbing Zhang,[b]* Jian Wang [a]*

[a] *Department of Chemistry and Biochemistry, Wichita State University, Wichita, Kansas 67260, United States*

[b] *College of Chemistry and Environmental Science, Hebei University, Key Laboratory of Analytical Science and Technology of Hebei Province, Baoding 071002, China*

[c] *Department of Mechanical Engineering, Wichita State University, Wichita, Kansas 67260, United States*

Abstract

Pb$_3$P$_2$S$_8$ was structurally characterized three decades ago with a second harmonic generation response reported. In this work, Pb$_3$P$_2$S$_8$ was revisited to investigate its electronic structure via DFT calculations and optical properties by UV-Vis measurements, second harmonic generation tests, laser damage threshold tests, and photocurrent measurements. Pb$_3$P$_2$S$_8$ is constructed by [PbS$_7$] polyhedra and [PS$_4$] tetrahedra, which was supported by crystal orbital Hamilton population (COHP) calculations. The electron localization function (ELF) simulations revealed the dominantly covalent and ionic bonding nature of P-S interactions and Pb-S interactions, respectively, which are both strongly polarized. Pb$_3$P$_2$S$_8$ is an indirect n-type semiconductor of 1.8 eV and 2.4(1) eV which are obtained from DFT calculations and UV-Vis measurements, respectively. Pb$_3$P$_2$S$_8$ is a non-type-I phase matching material with a good balance of second harmonic generation (SHG) and laser damage threshold (LDT) of 3.5×AGS and 2.6×AGS,

respectively (SHG based on 38-50 µm particle size sample). $Pb_3P_2S_8$ exhibits an intriguing photocurrent response of 45 µA cm^{-2} under light irradiation. $Pb_3P_2S_8$ is a new multifunctional material combining a nonlinear optical response and photocurrent response.

Introduction

Thiophosphates, a class of materials combining sulfur and phosphorus, have attracted growing attention due to their broad structural flexibility and intriguing physical applications. In **Figure 1**, various selected $[P_xS_y]$ structure units including $[PS_4]^{3-}$ [1], $[PS_5]^{5-}$ [2], $[P_2S_6]^{2-}$ [3], $[P_2S_6]^{4-}$ [4], $[P_2S_7]^{4-}$ [4], $[P_2S_{10}]^{4-}$ [5], $[P_3S_9]^{3-}$ [6], $[P_3S_{10}]^{5-}$ [7], and $[P_4S_{12}]^{4-}$ [8] are shown, where $[PS_4]^{3-}$ and $[P_2S_6]^{4-}$ are most common. The flexible $[P_xS_y]$ structure units interact with cations (main group elements or transition metals) to generate broad structural variety, spanning from 0D clusters to 3D frameworks [1-18]. The structural flexibility provides a fruitful land for emerging applications, such as nonlinear optical materials [19-25], ion conductors [26-35], hydrogen evolution [36, 37], and photocurrent response [38].
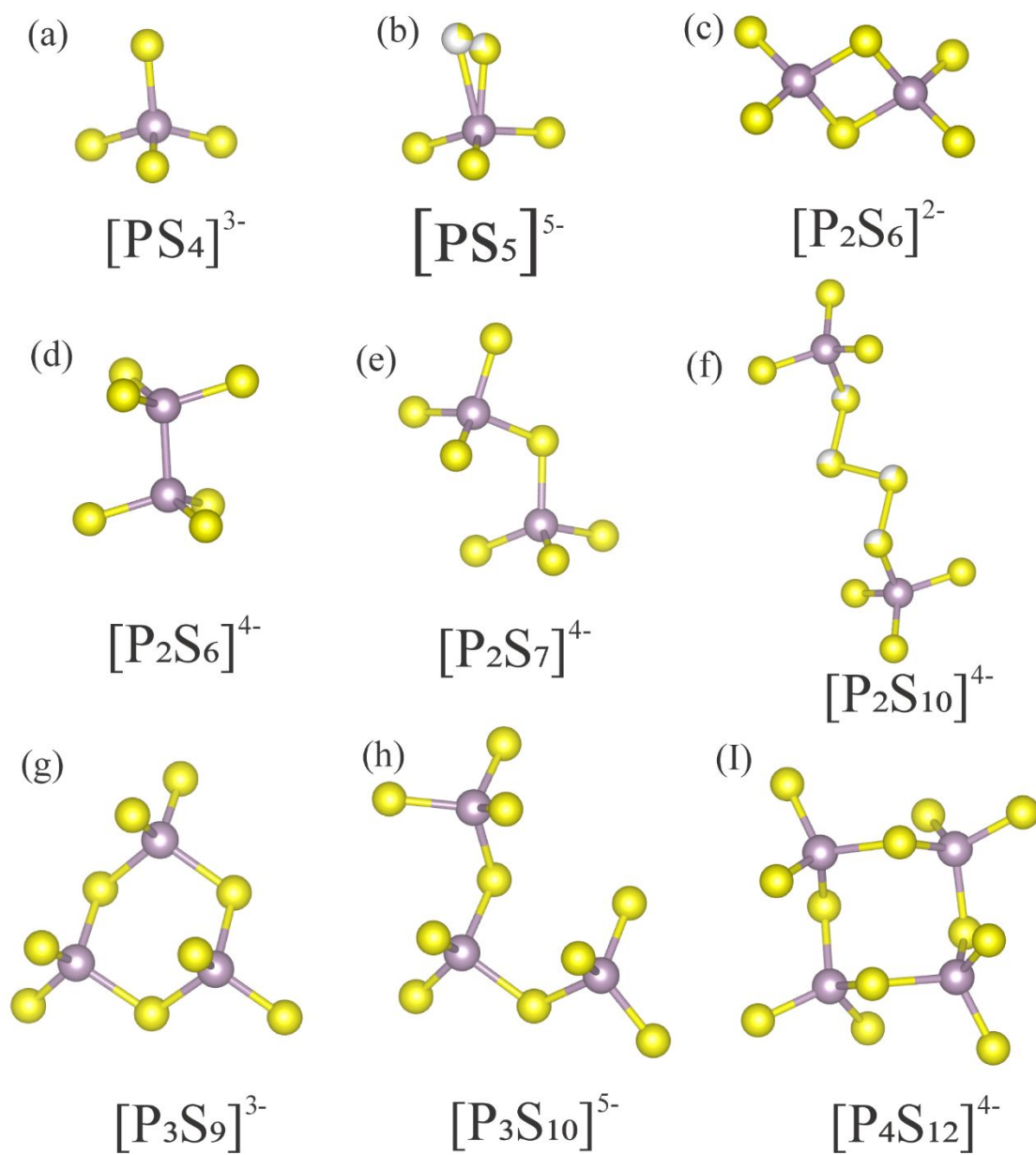
Figure 1. The selected $[P_xS_y]$ motifs demonstrate the structural flexibility of thiophosphates. P: gray color, S: yellow color.

$Pb_3P_2S_8$ was firstly structurally characterized by Kraemer, V. et al [39]. Later on, Voroshilov, Y.V. et al confirmed the acentric structure of $Pb_3P_2S_8$ during their exploration of the Pb-P-S phase diagram [40]. A second harmonic response of $Pb_3P_2S_8$ of $2 \times SiO_2$ was reported [39]. To our best

knowledge, the detailed physical properties and electronic structure studies of $Pb_3P_2S_8$ were not investigated. A theory study predicted that $Pb_3P_2S_8$ possesses potential good second harmonic generation response [24]. $Pb_3P_2S_8$ has attracted our interest due to its "simple" acentric crystal structure and easy to grow large crystals. In this work, mm-sized crystals of $Pb_3P_2S_8$ were grown via vapor transport reactions. The DFT calculation was employed to study the electronic structure of $Pb_3P_2S_8$. The chemical bonding of $Pb_3P_2S_8$ was pictorially understood by the crystal orbital Hamilton population (COHP) method and electron localization function (ELF). $Pb_3P_2S_8$ was revealed to be a good multifunctional material combining a nonlinear optical response and photocurrent response.

Experiments

Synthesis: All starting materials were stored and used in an Ar-filled glove box. Starting materials were used as received without any purification: Pb granules (Alfa Aesar, 99.gg%), P powder (Alfa Aesar, 99.5%), S powder (Alfa Aesar, 99.5%), I_2 (Fisher, 99.8%). The mm-sized crystals of $Pb_3P_2S_8$ were grown by a two-step vapor transport reaction. First step: The reactant elements were loaded into carbonized silica ampules at a molar ratio of Pb:P:S = 3:2:8 (total 2g) with ~0.1 g I_2 added as a vapor transport agent into a quartz tube of ~ Ø11mm×500 mm. The ampules were flame sealed under a high vacuum and placed in a programmable furnace. The ampules were heated to 923K in 48h, held at that temperature for 48h, and then cooled to 373K in 24h. Second step: the same tube from the first step was transferred to a gradient furnace with a 100K difference between the hot side and cold side. The material side was placed in the hot temperature zone with the empty top side located in the cold zone. For the hot end, the tube was heated to 923K in 48h, held at that temperature for 120 h, and then cooled to 373K in 120h. Many yellow-orange crystals of $Pb_3P_2S_8$ were found after the second step, which are shown in **Figure 3** insert. The sample was identified

as a single-phase sample shown in **Figure 2** (powder X-ray diffraction) and **Table S1** (single crystal X-ray diffraction).
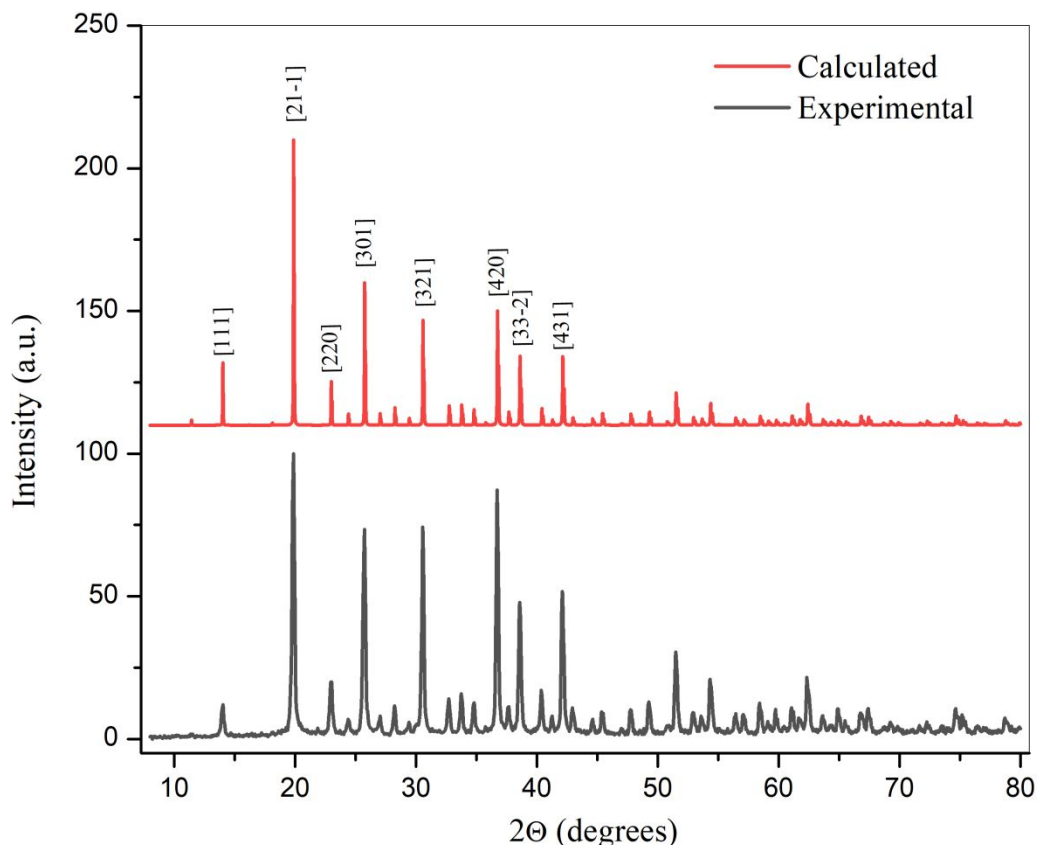

Figure 2. The powder X-ray diffraction pattern of $Pb_3P_2S_8$ with theory simulated pattern[39].

Powder X-ray Diffraction and Single crystal X-ray diffraction: Data were recorded at room temperature using a Rigaku Mini Flex II diffractometer with Cu-$K\alpha$ radiation (λ =1.5406 Å). To eliminate the particle orientation, the $Pb_3P_2S_8$ were ground with amorphous SiO_2 first then run a powder X-ray diffraction measurement. To validate the phase purity of our synthesized samples, single crystal data were collected using a Bruker Kappa APEX II diffractometer with graphite monochromated Mo-$K\alpha$ radiation (λ =0.71073 Å). The single crystal X-ray diffraction confirmed the same structure model with previous work (Table S1) [39].

UV-Vis Measurements: Diffuse-reflectance spectra were collected at room temperature by a PERSEE-T8DCS UV-Vis spectrophotometer equipped with an integration sphere in the wavelength range of 230−850 nm. The reflectance data, R, were recorded and converted to the Kubelka-Munk function, $f(R)=(1-R)^2(2R)^{-1}$. Tauc plots, $(KM*E)^2$ and $(KM*E)^{1/2}$, were applied to estimate direct and indirect bandgap, respectively. There are strong absorption edges detected for $Pb_3P_2S_8$ around 475-525 nm (**Figure S1**). The direct and indirect bandgaps of $Pb_3P_2S_8$ estimated by Tauc plots are 2.6(1) eV and 2.4(1) eV, respectively, which are shown in **Figure 3**.
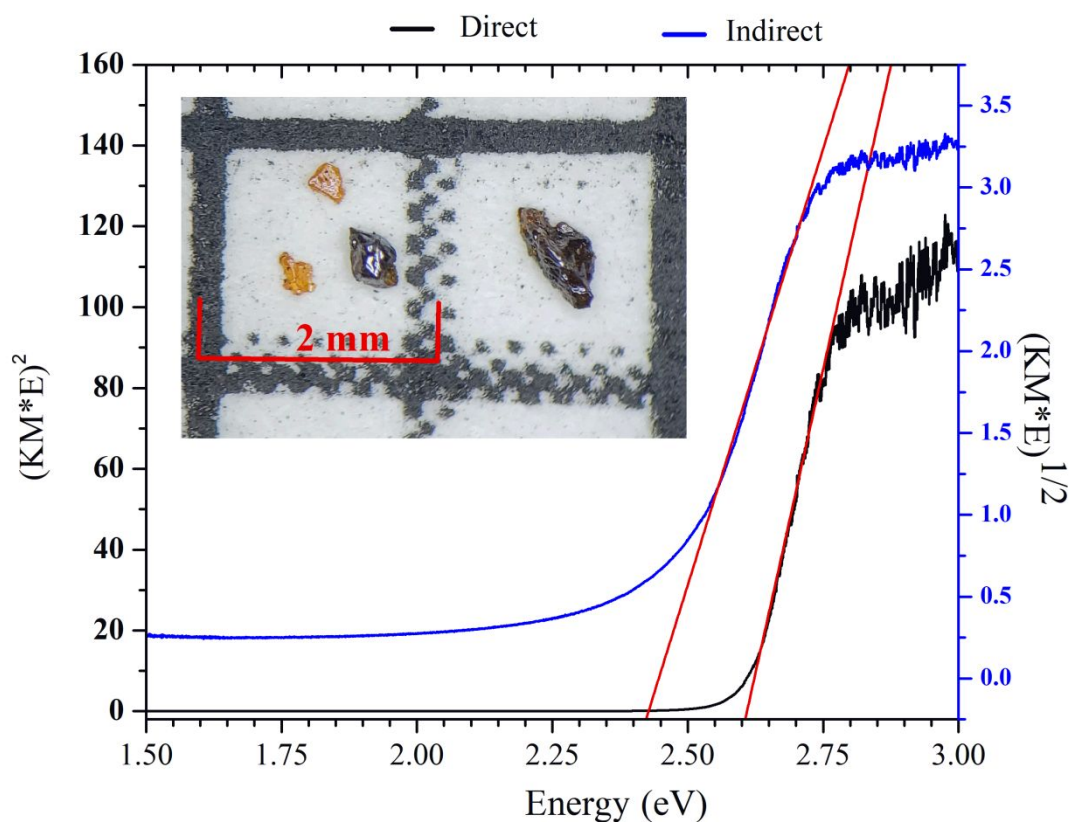

Figure 3. Tauc plot for allowed direct and indirect transitions of $Pb_3P_2S_8$. The insert shows a photo of selected $Pb_3P_2S_8$ crystals on 2 mm scale paper.

Theory Calculations: The partial density of states (PDOS), density of states (DOS), band structure, crystal orbital Hamilton population (COHP) method, and electron localization function

(ELF) are calculated using the tight binding-linear muffin tin orbitals-atomic sphere approximation

(TB-LMTO-ASA) program.[41, 42] The Barth-Hedin exchange potential was employed for the LDA

calculations. [42] The radial scalar-relativistic Dirac equation was solved to obtain the partial waves.

The basis set used contained Pb ($6s,6p$), P($3s,3p$), and S($3s,3p$) orbitals, and was employed for a

self-consistent calculation, with Pb($6d, 5f$), P ($3d$), and S($3d$) functions being downfolded. The

density of states and band structures were calculated after converging the total energy on a dense

k-mesh of $16\times16\times16$ points with 504 irreducible k-points. HSE gap (Eg-HSE) is calculated by

performing the DFT plane-wave code PWmat. [43] The optical properties were calculated based on

ab initio calculations implemented in the CASTEP package through density functional theory

(DFT).[44, 45.] The generalized gradient approximation (GGA)[46.] was adopted, and the

Perdew−Burke−Ernzerhof (PBE)[47] function was chosen to calculate the exchange-correlation

potential, with an energy cutoff of 820 eV. The numerical integration of the Brillouin zone was

performed using a $2 \times 2 \times 2$ Monkhorst−Pack k-point sampling. The geometry optimizations were

applied prior to property calculations. Second-order susceptibility $\chi(2)$ tensors are calculated by

the formula developed by Lin and Lee et al.[48,49].

SHG Measurement and LDT Test:

The pre-synthesized $Pb_3P_2S_8$ crystals and $AgGaS_2$ crystals (as the reference) were ground and

sieved into different particle sizes, including $38−55$, $55−88$, $88−105$, $105−150$, $150−200$, and

$200−250$ μm. Through a modified Kurtz and Perry method,[50] powder SHG responses of the title

$Pb_3P_2S_8$ and $AgGaS_2$ were investigated by a Q-switch laser (2.09 μm, 3 Hz, 50 ns). The LDTs of title compounds were evaluated on powder samples (150−200 μm) with a pulsed YAG laser (1.06 μm, 10 ns, 10 Hz). A similar size of $AgGaS_2$ is chosen as the reference. The judgment criterion is as follows: with increasing laser energy, the color change of the powder sample is constantly observed by an optical microscope to determine the damage threshold. To adjust different laser beams, an optical concave lens is added into the laser path. The damage spot is measured by the scale of the optical microscope.

Photocurrent response test: The photoanode was prepared via coating the $Pb_3P_2S_8$ thin film on the Fluorine-doped Tin Oxide (FTO) glass by the doctor blade method. The photoelectrochemical performance of the photoanode was evaluated in a typical three-electrode configuration, consisting of a $Pb_3P_2S_8$ photoanode as the working electrode, Pt as the counter electrode, and Ag/AgCl as the reference electrode. 0.1M Na_2SO_4 aqueous solution was used as the electrolyte. Linear sweep voltammetry and I-t scans were collected on the electrochemical workstation (Gamry Interface 5000) under illumination of AM 1.5 (1 sun, 100 mW/cm^2) using a solar simulator (Newport).

Results and Discussion

Crystal growth and Crystal Structure. $Pb_3P_2S_8$ crystals were discovered by vapor transport reactions. The previous study claimed the discovery of red-colored well facetted tetrahedral crystals with maximum edge lengths of 1 mm [39]. Our synthesis generated yellow-colored, irregularly shaped crystals of $Pb_3P_2S_8$ (**Figure 3** insert). There are strong absorption edges around 475-525 nm detected by the solid-state UV-Vis spectrum (**Figure S1**), which might correspond to the yellow-orange color of $Pb_3P_2S_8$. Both single-crystal X-ray diffraction and powder X-ray diffraction verified that $Pb_3P_2S_8$ crystallizes in space group *P2$_1$3* (No.198) with unitcell parameters

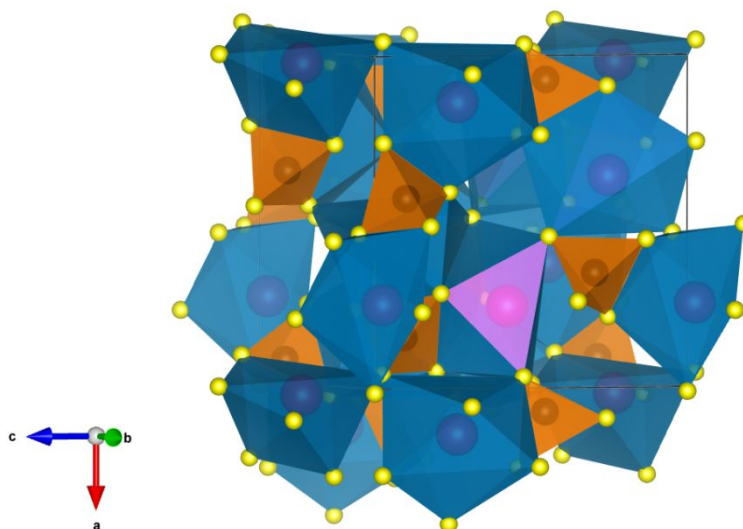of a=10.9253(10) Å, which is isostructural to Kraemer, V.'s and Voroshilov, Y.V.'s structural model [39, 40].

Figure 4. The polyhedral models of the unitcell of $Pb_3P_2S_8$ viewing down the [010] direction. La: red color, P: black color; S: yellow color. $[PbS_7]$ polyhedra shown in dark blue, $[PS_4]$ tetrahedra shown in orange.

Kraemer, V. et al and Voroshilov, Y.V. et al described their structural models constructed by $[PbS_8]$ polyhedra and $[PS_4]$ tetrahedra. The Pb-S interactions within $[PbS_8]$ polyhedra fall into the range of 2.883-3.468 Å. The P-S interactions within $[PS_4]$ tetrahedra are 2.031-2.065 Å. Our COHP calculations revealed weak bonding of 3.468 Å Pb-S interactions (*vide infra*), which is also longer than various reported lead-sulfides such as $Pb_9Sb_8S_{21}$(2.460-3.117) [51], $PbGa_2GeS_6$(2.849-3.111)[52], $TlPbAsS_3$(2.906-3.228)[53], $Ag_7PbP_3S_{12}$(2.809-3.303)[54], $Pb_2P_2S_6$(2.899-3.204)[55], $RbPbPS_4$(2.921-3.282)[56], $KPbPS_4$(2.924-3.180)[57], $Na_6Pb_3P_4S_{16}$(2.831-3.224)[58], etc. Hence we conclude that the crystal structure of $Pb_3P_2S_8$ is built by $[PbS_7]$ polyhedra interconnected by $[PS_4]$ tetrahedra.

DFT Calculations

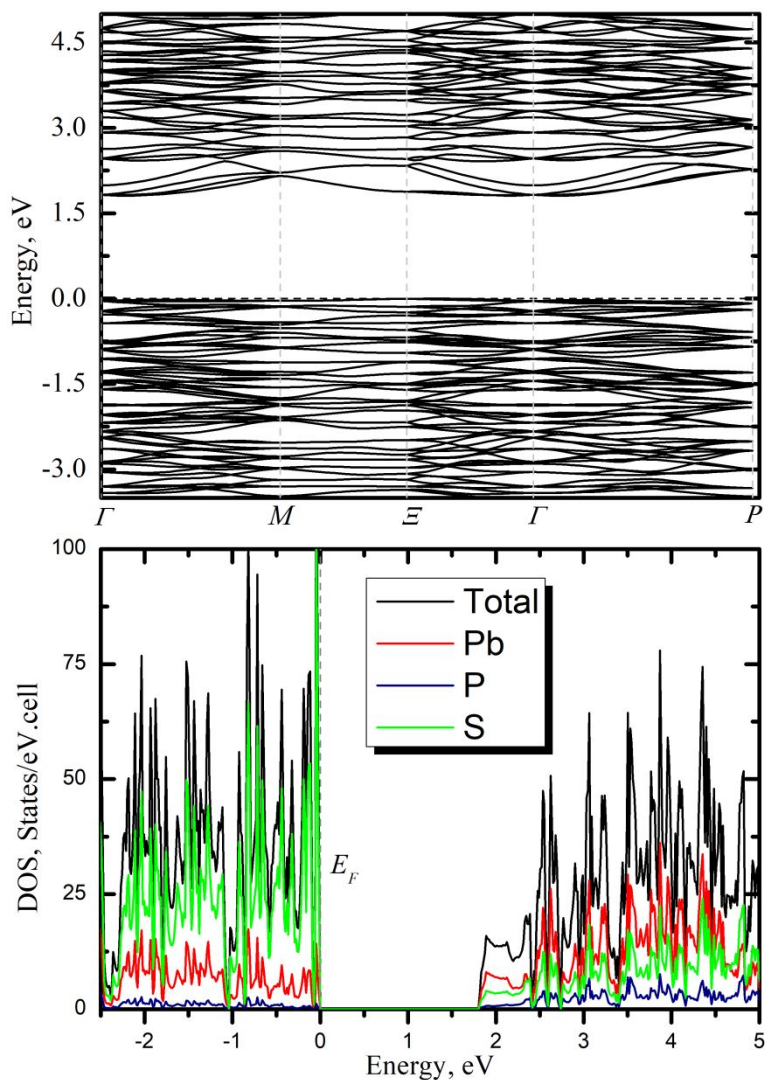**Figure 5.** (top) Band structure and (bottom) density of states of $Pb_3P_2S_8$.

The charge-balanced formula $(Pb^{2+})_3(P^{5+})_2(S^{2-})_8$ can be established by assigning a formal charge of 2+ to the Pb atoms, 5+ to the P atoms, and 2- to the S atoms due to the absence of any homoatomic interactions. The Pb^{2+} is verified by the presence of $6p^2$ lone pair electrons elucidated by ELF calculations (*vide infra*). The oxidation state of lead atoms of 2+ was validated by bond valence sum calculations [59-61]. Bond valence sum calculations concluded that the BVS of Pb

atoms and P atoms to be 1.98 and 4.95 receptivity, which suggests Pb atoms and P atoms with

oxidation 2+ and 5+ respectively. The semiconductor nature of $Pb_3P_2S_8$ was confirmed by DFT

calculations and UV-Vis measurements (**Figure 3**). From **Figure 5** a (top), the top of the valance

band is located between Γ points and Ξ points with the bottom of the conduction band located at

Γ points. Hence, $Pb_3P_2S_8$ is predicted to be an indirect semiconductor with a bandgap of 1.8 eV,

which is lower than the measured value of 2.4(1) eV (**Figure 3**). The underestimation of bandgap

by DFT calculation is well known [62]. To better estimate the band structure of $Pb_3P_2S_8$, the HSE

bandgap of $Pb_3P_2S_8$ was calculated, which is shown in Figure S2. The HSE bandgap calculation

verified our prediction of indirect semiconductor nature of $Pb_3P_2S_8$. The bandgap established for

HSE calculation is 2.77 eV, which are close to the measured value of 2.4(1) eV via UV-Vis.

(**Figure 3**).   The top of the valance band exhibits small dispersion along $\Xi \rightarrow \Gamma$ direction. There is

stronger dispersion present at the bottom of the conduction band along with $\Gamma \rightarrow M$ and $\Gamma \rightarrow P$

directions. In $Pb_3P_2S_8$, the top of the valance band is mainly contributed by S $3p$ orbitals with

certain contributions of Pb $6p$ orbitals. The major contribution of the bottom of the conduction

band is from S $3p$ orbitals with certain contributions of Pb $6p$ orbitals. Interestingly, P $3p$ orbitals

have minimum contributions to the top of the valence band and the bottom of the conduction band.

The charge distribution of the bottom of the conduction band and the top of the valence band were

also calculated, which are exhibited in Figure S3. The charge distribution of the top of valance

band is non-bonding 3p orbitals of S atoms   （Figure S3 right). The charge distribution of

the bottom of conduction band are anti-sigma bonds in PS_4 and 6p orbitals of Pb atoms (Figure S3

left). Hence, the optical properties of $Pb_3P_2S_8$ are expected to be controlled by Pb-S interactions.

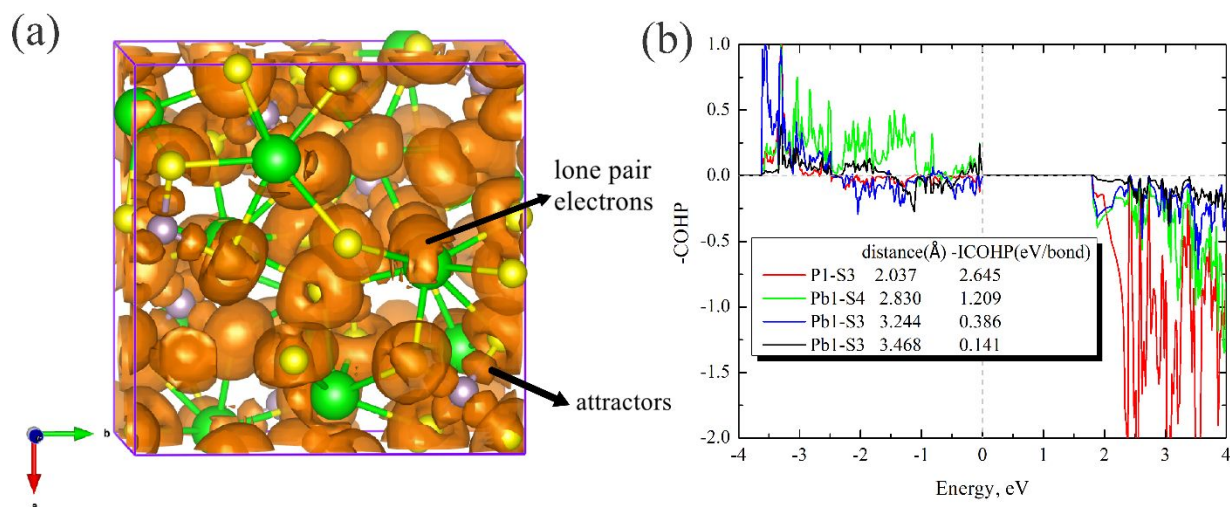**Figure 6.** (a) 3D isosurfaces of the electron localization function (ELF) for $Pb_3P_2S_8$ with η=0.75, Pb: green color, P: gray color, S: yellow color (b): Crystal Orbital Hamilton Population (COHP) analyses of the selected Pb-S interactions and P-S interactions.

ELF calculations and COHP calculations were employed to study the bonding picture of $Pb_3P_2S_8$, which are presented in **Figure 6** a and **Figure 6** b respectively. The ELF maxima isosurfaces capping the Pb atoms correspond to the $6s^2$ electron lone pairs on Pb. The presence of lone pair electrons confirms the oxidation state of Pb should be +2. As **Figure 6a** shows, there are clear "attractors" (ELF maxima between atoms) between P and S. Hence the P-S interactions are expected to mainly have covalent character. In contrast, the ELF isosurfaces are mostly spherical around the S atoms for Pb-S interactions, which indicates the Pb-S bonds possess certain ionic characteristics. The COHP calculations prove that both Pb-S bonds and P-S bonds are strongly bonding (*vide infra*). Both Pb-S bonds and P-S bonds are highly polarized. The COHP calculations found a strong bonding character for 2.037 Å P-S interactions with calculated –ICOHPs of 2.645 eV/bond. The P-S interactions are not well-optimized with certain antibonding characters between -2.5 eV to the Fermi level, with the essentially nonbonding interactions just above the Fermi level,

0-1.8 eV and strong antibonding character found for interactions at higher energies. We propose that this may account for the flexibility of structural chemistry of $[P_xS_y]$ units, which are shown in **Figure 1**. The shortest Pb-S interactions of 2.830 Å are strongly bonding with –ICOHPs of 1.209 eV/bond. The calculated –ICOHPs of 0.386 eV/bond for the 3.244Å Pb-S points out weak but accountable bonding characters. The 3.468 Å Pb-S interactions are too far from each other to be counted as bonding interactions with calculated –ICOHPs of 0.141 eV/bond. The COHP calculations help clarify that the Pb atoms are surrounded by seven S atoms instead of previously reported eight S atoms. [39, 40]

Nonlinear Optical Properties.

The SHG and LDT were measured on the grown high-quality single crystals. $Pb_3P_2S_8$ exhibits a good LDT of 2.6 × $AgGaS_2$ (AGS) (**Table S2**). The SHG tests revealed $Pb_3P_2S_8$ is not a type-I phase-matching material with SHG intensity decreasing as particle size increases, as shown in **Figure 7**. For the sample of 38-55 μm particle size, $Pb_3P_2S_8$ shows a high SHG response of 3.5 × AGS. The second-order nonlinear susceptibility $\square^{123}$ of $Pb_3P_2S_8$ was calculated to be 20.22 pm/V. The previous work also detected a SHG response of 2×SiO_2 using a 1064 nm laser [39]. $Pb_3P_2S_8$ is not a type-I phase matching material, but possesses a good balance between SHG and LDT.
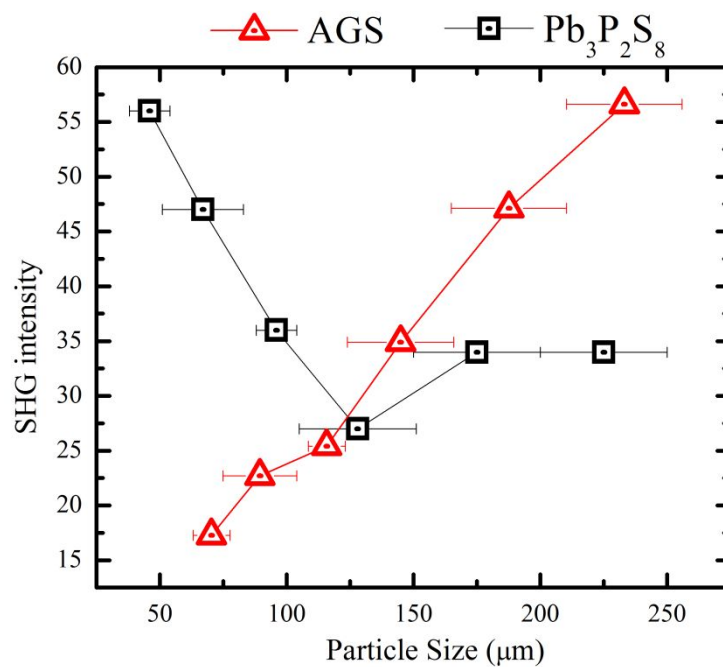
Figure 7. SHG intensities of $Pb_3P_2S_8$ and $AgGaS_2$ were measured on variable particle size samples utilizing a 2.09 µm laser.
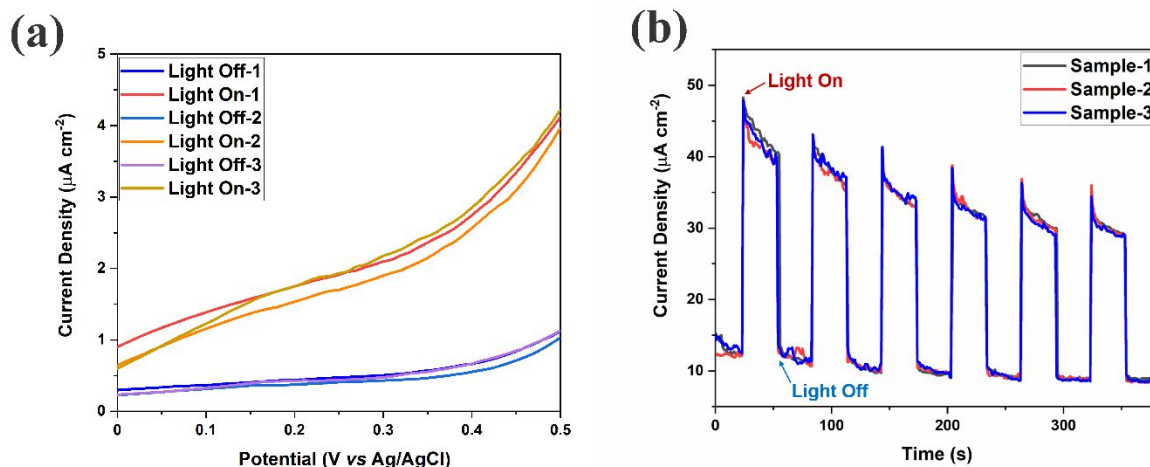
Photocurrent response test

Figure 8. (a) PEC photocurrent-potential (I-V) curves. (b) Photocurrent density-time for $Pb_3P_2S_8$ photoanode. There samples were tested to demonstrate good data reproducibility.

Figure 8a shows the linear sweep voltammetry with a scan rate of 10 mV s^{-1} for $Pb_3P_2S_8$ film. The current density of $Pb_3P_2S_8$ film is 3.68 μA cm^{-2} under light irradiation, while it is almost zero without light irradiation at 0.5 V *vs* Ag/AgCl. **Figure 8**b plots the periodic on/off transient photocurrent response of $Pb_3P_2S_8$ film under intermittent simulated solar light, where several repeatable on-off cycles indicate $Pb_3P_2S_8$ is an n-type semiconductor. The slow decay of photocurrent was due to the photocorrosion of a sulfide photocatalyst [63, 64]. The photocurrent density of $Pb_3P_2S_8$ (45 μA cm^{-2}) is much higher than many sulfide compounds, such as $Rb_2CuSb_7S_{12}$(10 μA cm^{-2})[65], $BaCuSbS_3$(55 nA cm^{-2})[66], $Rb_2Ba_3Cu_2Sb_2S_{10}$(6 nA cm^{-2})[67], etc. The superior photocurrent density suggests efficient separation and migration of photo-excited electron-hole charge carriers of $Pb_3P_2S_8$ film. To elucidate the superior photocurrent properties of $Pb_3P_2S_8$, the measurements of carrier mobility of $Pb_3P_2S_8$ are essential and undergoing.

Conclusions:

$Pb_3P_2S_8$ was revisited and discovered to be a new multifunctional material. Both intriguing SHG response and photocurrent response were detected in $Pb_3P_2S_8$. High quality single crystals of $Pb_3P_2S_8$ were grown by a two-step vapor transport reaction. $Pb_3P_2S_8$ is an indirect bandgap semiconductor of 2.4(1) eV, which is verified by DFT calculations and UV-Vis measurements. Both strong covalent and ionic bonding interactions exist in $Pb_3P_2S_8$ for P-S bonds and Pb-S bonds, respectively. $Pb_3P_2S_8$ possesses a good balance between SHG (3.5 × AGS based on a sample of 38-55 µm particle size) and LDT (2.6× AGS). A superior photocurrent density of $Pb_3P_2S_8$ was detected of 45 µA cm^{-2} under light irradiation. The high photocurrent response and good SHG response coupled with cheap constituting elements, simple crystal structure, easy to grow crystals, and good stability guarantees $Pb_3P_2S_8$ as a new multifunctional material. There were about 645 thiophosphate compounds reported in the ICSD with less than 20% thoroughly studied, which may be a new platform for exploring multifunctional materials.

ASSOCIATED CONTENTS

Supporting Information

The refined crystallographic data, KM UV-Vis plots, LDT measurements.

Corresponding author:

Jian Wang   jian.wang@wichita.edu

Notes

The authors declare no competing financial interest.

References:

[1]   S. Jörgens, D. Johrendt and A. Mewis, *Zeitschrift für anorganische und allgemeine Chemie*, 2002, **628**, 1765.

[2]   F. Alahmari, B. Davaasuren, J. Khanderi and A. Rothenberger, *Z. Anorg. Allg. Chem.*, 2016, **642**, 361–367.

[3]   P. Grenouilleau, R. Brec, M. Evain, and J. Rouxel, *Rev. Chim. Miner.,*1983, **20**, 628-635.

[4]   S. Jörgens, A. Mewis, R.-D. Hoffmann, R. Pöttgen and B. D. Mosel, *Z. Anorg. Allg. Chem.*, 2003, **629**, 429–433.

[5]   J. A. Hanko, J. Sayettat, S. Jobic, R. Brec and M. G. Kanatzidis, *Chem. Mater.*, 1998, **10**, 3040–3049.

[6]   J. A. Aitken, C. Canlas, D. P. Weliky and M. G. Kanatzidis, *Inorg. Chem.*, 2001, **40**, 6496–6498.

[7]   R. F. Hess, K. D. Abney, J. L. Burris, H. D. Hochheimer and P. K. Dorhout, *Inorg. Chem.*, 2001, **40**, 2851–2859.

[8]   M. Evain, R. Brec, G. Ouvrard and J. Rouxel, *Mater. Res. Bull.*, 1984, **19**, 41–48.

[9]   V. V. Klepov and H.-C. Zur Loye, *Inorg. Chem.*, 2018, **57**, 11175–11183.

[10]   A. R. Wildes, V. Simonet, E. Ressouche, R. Ballou and G. J. McIntyre, *J. Phys. Condens. Matter*, 2017, **29**, 455801.

[11]   L. M. Schoop, R. Eger, R. K. Kremer, A. Kuhn, J. Nuss and B. V. Lotsch, *Inorg. Chem.*, 2017, **56**, 1121–1131.

[12]   C. B. Dressel, W. Klein and T. F. Fässler, *Z. Anorg. Allg. Chem.*, 2017, **643**, 1814–1817.

[13]   L. M. Schoop, R. Eger, J. Nuss, F. Pielnhofer and B. V. Lotsch, *Z. Anorg. Allg. Chem.*, 2017, **643**, 1818–1823.

[14]   A. Mesbah, J. Prakash, D. Rocca, S. Lebègue, J. C. Beard, B. A. Lewis and J. A. Ibers, *J. Solid State Chem.*, 2016, **233**, 217–220.

[15]   A. Rothenberger, C. Morris and M. G. Kanatzidis, *Inorg. Chem.*, 2010, **49**, 5598–5602.

[16]   S. Banerjee, J. M. Szarko, B. D. Yuhas, C. D. Malliakas, L. X. Chen and M. G. Kanatzidis, *J. Am. Chem. Soc.*, 2010, **132**, 5348–5350.

[17]   D. G. Chica, A. K. Iyer, M. Cheng, K. M. Ryan, P. Krantz, C. Laing, R. Dos Reis, V. Chandrasekhar, V. P. Dravid and M. G. Kanatzidis, *Inorg. Chem.*, 2021, **60**, 3502–3513.

[18]   J. A. Aitken and M. G. Kanatzidis, *Inorg. Chem.*, 2001, **40**, 2938–2939.

[19]   J. Feng, C.-L. Hu, B. Li and J.-G. Mao, *Chem. Mater.*, 2018, **30**, 3901–3908.

[20]   Y.-H. Fan, X.-M. Jiang, B.-W. Liu, S.-F. Li, W.-H. Guo, H.-Y. Zeng, G.-C. Guo and J.-S. Huang, *Inorg. Chem.*, 2017, **56**, 114–124.

[21]   C. D. Morris, I. Chung, S. Park, C. M. Harrison, D. J. Clark, J. I. Jang and M. G. Kanatzidis, *J. Am. Chem. Soc.*, 2012, **134**, 20733–20744.

[22]   Z. Li, J. Yao and Y. Wu, *Cryst. Growth Des.*, 2020, **20**, 7550–7564.

[23]   I. Chung and M. G. Kanatzidis, *Chem. Mater.*, 2014, **26**, 849–869.

[24]   L. Kang, M. Zhou, J. Yao, Z. Lin, Y. Wu and C. Chen, *J. Am. Chem. Soc.*, 2015, **137**, 13049–13059.

[25]   Z. Li, S. Zhang, W. Xing, Y. Guo, C. Li, Z. Lin, J. Yao and Y. Wu, *J. Mater. Chem. C Mater. Opt. Electron. Devices*, 2020, **8**, 5020–5024.

[26]   T. Krauskopf, S. P. Culver and W. G. Zeier, *Inorg. Chem.*, 2018, **57**, 4739–4744.

[27]   T. Krauskopf, S. P. Culver and W. G. Zeier, *Chem. Mater.*, 2018, **30**, 1791–1798.

[28]   M. Duchardt, S. Neuberger, U. Ruschewitz, T. Krauskopf, W. G. Zeier, J. Schmedt auf der Günne, S. Adams, B. Roling and S. Dehnen, *Chem. Mater.*, 2018, **30**, 4134–4139.

[29]   K. Kaup, F. Lalère, A. Huq, A. Shyamsunder, T. Adermann, P. Hartmann and L. F. Nazar, *Chem. Mater.*, 2018, **30**, 592–596.

[30]   T. Bernges, S. P. Culver, N. Minafra, R. Koerver and W. G. Zeier, *Inorg. Chem.*, 2018, **57**, 13920–13928.

[31]   M. Duchardt, U. Ruschewitz, S. Adams, S. Dehnen and B. Roling, *Angew. Chem. Int. Ed Engl.*, 2018, **57**, 1351–1355.

[32]   Y.-H. Fan, H.-Y. Zeng, X.-M. Jiang, M.-J. Zhang, B.-W. Liu, G.-C. Guo and J.-S. Huang, *Inorg. Chem.*, 2017, **56**, 962–973.

[33]   C. Dietrich, D. A. Weber, S. Culver, A. Senyshyn, S. J. Sedlmaier, S. Indris, J. Janek and W. G. Zeier, *Inorg. Chem.*, 2017, **56**, 6681–6687.

[34]   M. A. Kraft, S. P. Culver, M. Calderon, F. Böcher, T. Krauskopf, A. Senyshyn, C. Dietrich, A. Zevalkink, J. Janek and W. G. Zeier, *J. Am. Chem. Soc.*, 2017, **139**, 10909–10918.

[35]   Y. Sun, K. Suzuki, S. Hori, M. Hirayama and R. Kanno, *Chem. Mater.*, 2017, **29**, 5858–5864.

[36]   T. Wu, M. L. Stone, M. J. Shearer, M. J. Stolt, I. A. Guzei, R. J. Hamers, R. Lu, K. Deng, S. Jin and J. R. Schmidt, *ACS Catal.*, 2018, **8**, 1143–1152.

[37]   X. Zhang, Z. Luo, P. Yu, Y. Cai, Y. Du, D. Wu, S. Gao, C. Tan, Z. Li, M. Ren, T. Osipowicz, S. Chen, Z. Jiang, J. Li, Y. Huang, J. Yang, Y. Chen, C. Y. Ang, Y. Zhao, P. Wang, L. Song, X. Wu, Z. Liu, A. Borgna and H. Zhang, *Nat. Catal.*, 2018, **1**, 460–468.

[38]   V. Itthibenchapong, R. S. Kokenyesi, A. J. Ritenour, L. N. Zakharov, S. W. Boettcher, J. F. Wager and D. A. Keszler, *J. Mater. Chem. C Mater. Opt. Electron. Devices*, 2013, **1**, 657–662.

[39]   E. Post and V. Krämer, *Mater. Res. Bull.*, 1984, **19**, 1607–1612.

[40]   I.P. Prits, M.V. Potorii and Yu.V. Voroshilov, *Sov. Prog. Chem.*1989,**55**, 25-27.

[41]   O. Jepsen, A. Burkhardt and O. K Andersen, *The Program TB-LMTO-ASA, Version4.7*, Max-Planck-Institut für Festkörperforschung, Stuttgart, Germany, 1999.

[42]   U. von Barth and L. Hedin, *J. phys.*, 1972, **5**, 1629–1642.

[43]   W. Jia, J. Fu, Z. Cao, L. Wang, X. Chi, W. Gao and L.-W. Wang, *J. Comput. Phys.*, 2013, **251**, 102–115.

[44]   W. Jia, Z. Cao, L. Wang, J. Fu, X. Chi, W. Gao and L.-W. Wang, *Comput. Phys. Commun.*, 2013, **184**, 9–18.

[45]   B. G. Pfrommer, M. Côté, S. G. Louie and M. L. Cohen, *J. Comput. Phys.*, 1997, **131**, 233–240.

[46]   J. P. Perdew, K. Burke and M. Ernzerhof, *Phys. Rev. Lett.*, 1997, **78**, 1396–1396.

[47]   A. M. Rappe, K. M. Rabe, E. Kaxiras and J. D. Joannopoulos, *Phys. Rev. B Condens. Matter*, 1990, **41**, 1227–1230.

[48]   J. Lin, M.-H. Lee, Z.-P. Liu, C. Chen and C. J. Pickard, *Phys. Rev. B Condens. Matter*, 1999, **60**, 13380–13389.

[49]   B. Zhang, M.-H. Lee, Z. Yang, Q. Jing, S. Pan, M. Zhang, H. Wu, X. Su, C.-S. Li, *Appl. Phys. Lett.*, 2015, **106**, 031906.

[50]   S. K. Kurtz and T. T. Perry, *J. Appl. Phys.*, 1968, **39**, 3798–3813.

[51]   Y. Matsushita, *Z. Kristallogr. Cryst. Mater.*, 2018, **233**, 279–284.

[52]   Y.-Z. Huang, H. Zhang, C.-S. Lin, W.-D. Cheng, Z. Guo and G.-L. Chai, *Cryst. Growth Des.*, 2018, **18**, 1162–1167.

[53]   N. Meisser, P. Roth, F. Nestola, C. Biagioni, L. Bindi and M. Robyr, *Eur. j. mineral.*, 2017, **29**, 679–688.

[54]   Y.-H. Fan, H.-Y. Zeng, X.-M. Jiang, M.-J. Zhang, B.-W. Liu, G.-C. Guo and J.-S. Huang, *Inorg. Chem.*, 2017, **56**, 962–973.

[55]   R. Becker, W. Brockner and H. Schaefer, *Z. Naturforsch. A*. 1983, **38**, 874-879.

[56]   J. Yao and J. A. Ibers, *Acta Crystallogr. Sect. E Struct. Rep. Online*, 2004, **60**, i108–i110.

[57]   I. Belkyal, M. El Azhari, Y.-D. Wu, W. Bensch, K.-F. Hesse and W. Depmeier, *Solid State Sci.*, 2006, **8**, 59–63.

[58]   J. A. Aitken and M. G. Kanatzidis, *Inorg. Chem.*, 2001, **40**, 2938–2939.

[59]   N. E. Brese and M. O'Keeffe, *Acta Crystallogr. B*, 1991, **47**, 192–197.

[60]   N. A. Moroz, C. Bauer, L. Williams, A. Olvera, J. Casamento, A. A. Page, T. P. Bailey, A. Weiland, S. S. Stoyko, E. Kioupakis, C. Uher, J. A. Aitken and P. F. P. Poudeu, *Inorg. Chem.*, 2018, **57**, 7402–7411.

[61]   P. Wang, M. Abudoureheman and Z. Chen, *Dalton Trans.*, 2020, **49**, 17221–17229.

[62]   J. Wang, L.-L. Wang and K. Kovnir, *J. Mater. Chem. A Mater. Energy Sustain.*, 2018, **6**, 4759–4767.

[63]   B. Weng, M.-Y. Qi, C. Han, Z.-R. Tang and Y.-J. Xu, *ACS Catal.*, 2019, **9**, 4642–4687.

[64]   X. Ning and G. Lu, *Nanoscale*, 2020, **12**, 1213–1223.

[65]   Y. Xiao, S.-H. Zhou, R. Yu, Y. Shen, Z. Ma, H. Lin and Y. Liu, *Inorg. Chem.*, 2021, **60**, 9263–9267.

[66]   Z. Ma, F. Weng, Q. Wang, Q. Tang, G. Zhang, C. Zheng, R. P. S. Han and F. Huang, *RSC Adv.*, 2014, **4**, 28937.

[67]   C. Liu, Y. Xiao, H. Wang, W. Chai, X. Liu, D. Yan, H. Lin and Y. Liu, *Inorg. Chem.*, 2020, **59**, 1577–1581.